



# Design of achromatic augmented reality visors based on composite metasurfaces

ELYAS BAYATI,<sup>1,\*</sup>  ANDREW WOLFRAM,<sup>1</sup> SHANE COLBURN,<sup>1</sup> LUOCHENG HUANG,<sup>1</sup>  AND ARKA MAJUMDAR<sup>1,2</sup> 

<sup>1</sup>Department of Electrical and Computer Engineering, University of Washington, Seattle, Washington 98195, USA

<sup>2</sup>Department of Physics, University of Washington, Seattle, Washington 98195, USA

\*Corresponding author: [elyasb@uw.edu](mailto:elyasb@uw.edu)

Received 28 September 2020; revised 18 December 2020; accepted 22 December 2020; posted 23 December 2020 (Doc. ID 410895); published 22 January 2021

**A compact near-eye visor (NEV) system that can guide light from a display to the eye could transform augmented reality (AR) technology. Unfortunately, existing implementations of such an NEV either suffer from small field of view or chromatic aberrations. See-through quality and bulkiness further make the overall performance of the visors unsuitable for a seamless user experience. Metasurfaces are an emerging class of nanophotonic elements that can dramatically reduce the size of optical elements while enhancing functionality. In this paper, we present a design of composite metasurfaces for an ultracompact NEV. We simulate the performance of a proof-of-principle visor corrected for chromatic aberrations while providing a large display field of view ( $>77^\circ$  both horizontally and vertically) and good see-through quality [ $>70\%$  transmission and less than a wavelength root mean-square (RMS) wavefront error over the whole visible wavelength range] as needed for an immersive AR experience. © 2021 Optical Society of America**

<https://doi.org/10.1364/AO.410895>

## 1. INTRODUCTION

Augmented reality (AR) technology has recently attracted considerable attention and could revolutionize technologies ranging from applications in the military and navigation to education and entertainment. Using these devices, we can effectively integrate computer-generated virtual information into the real world. AR can be implemented in various ways, including smartphone displays, head-up displays (HUDs), and head-mounted displays (HMDs) [1]. Among the various approaches, see-through head-mounted near-eye displays (AR glasses) have been of primary focus because of their potential to provide an extremely high sense of immersion. One of the most vital components in a HMD is a near-eye visor (NEV). Current implementations of NEVs can be broadly classified into two categories: **reflection-based**, where light from a display placed near the eye is reflected off a freeform visor to enter the eye [2,3], and **waveguide-based**, where light is passed through a waveguide and projected to the eyes using a grating [4–6]. While reflective visors can provide higher efficiency and transparency, they are often bulky and suffer from a small eye box, and in general they need to be placed far away from the eyes to achieve a wide field of view (FOV). Waveguide-based NEVs can provide a much more compact form factor with sufficient eye-box expansion, although they often have lower FOV and efficiency. They also suffer from strong chromatic aberrations in both the image passed through the waveguide as well as in see-through mode,

as the gratings are diffractive in nature. The core of a waveguide NEV consists of the input and output couplers. These can be either simple prisms, microprism arrays, embedded mirror arrays [7], surface relief gratings [8], thin or thick holographic optical elements (HOEs) [6], or diffractive optical elements (DOEs) [5]. The outcoupling efficiency of the gratings is, however, low, making the energy efficiency of these waveguide-based visors poor relative to reflection-based visors. A closer look at reflective visors reveals that the trade-off between size and FOV of the NEV primarily originates from the fact that current NEVs rely on geometric reflections and refractions to bend light.

In recent years, subwavelength diffractive optics, commonly known as metasurfaces, have emerged as a versatile candidate to create ultrathin, flat optical elements [9]. These metasurfaces are quasiperiodic arrays of subwavelength optical antennas that can modify the phase, amplitude, or polarization of an incident optical wavefront. This enables the creation of arbitrary optical surfaces, including those for freeform optical elements [10]. Unlike conventional diffractive optics, the subwavelength scatterers in a metasurface preclude higher-order diffraction, resulting in higher efficiency, as all the light can be funneled into the zeroth order [11]. As diffraction can bend light by an angle more than reflection and refraction, it is possible to bring a metasurface closer to the eye while maintaining a wide FOV. Recently, the first silicon metasurface freeform visor was designed by our group [12], providing a large FOV for

virtual reality (VR) applications ( $77.3^\circ$  both horizontally and vertically) when placed only 2.5 cm away from the eye. This metasurface visor, however, severely distorts the real-world view, has strong chromatic aberrations, and is not transparent for AR applications. In addition to our group, several other metasurface-based visor designs have been reported in the literature for achieving large FOV, lighter designs, and better see-through quality, including designs based on combinations of a metalens and dichroic mirrors [13,14], Pancharatnam–Berry phase metalenses [15], and a compact light engine based on multilayer-metasurface optics [16].

In this paper, we propose a metasurface freeform optics-based NEV that will circumvent real-world distortions and eliminate chromatic aberrations as needed for an immersive AR experience. For this purpose, we propose to use a composite metasurface: one of the metasurfaces reflects light from the display to project the virtual world to the user's eye, while the second metasurface circumvents the distortion of the real world due to the first metasurface. The first metasurface is designed to have multi-chrome operation, in which two metasurfaces together preserve the color information in transmission. The resultant display FOV of the composite metasurface NEV is more than  $77^\circ$  both horizontally and vertically, which is better than that of current existing AR visors, and it also has acceptable see-through quality over the visible range (less than a wavelength RMS wavefront error).

## 2. PAIRED PHASE MASKS

First, we design and model the single metasurface NEV that can guide light from a display at the HMD to the human eye via ray optical simulation (ZEMAX-OpticStudio). The size of the visor is assumed to be  $4\text{ cm} \times 4\text{ cm}$  to maintain a compact form factor comparable to that of ordinary sunglasses while still having a large FOV when placed only 2.5 cm away from the eyes. The display is placed between the visor and the eye: 1 cm away and 1.5 cm upwards from the visor with an angle of  $45^\circ$  with respect to the optical axis. The display is initially assumed to be monochromatic (540 nm). The eye model that we use here for simulation is the widely accepted model proposed by Liou and Brennan [17]. Here it is assumed that the eye is looking out through an optical system, so the retina is the image surface. We model the visor phase mask with Zernike standard polynomials [18]. We find that the first six Zernike terms converge in a reasonable time and are sufficient to guide light from the display to the human eye in an acceptable manner. A schematic of a ray-tracing simulation from our reflective metasurface is shown in Fig. 1(A). The first metasurface (near the eye) will be partially reflective, and the design principle will follow the ray-tracing approach of sending light from each point on the display to the eye. The virtual display FOV from our simulation is estimated to be  $77.3^\circ$  along both vertical and horizontal directions. Figure 1(B) illustrates the reflective phase mask obtained from the Zernike standard polynomials from the first metasurface of our visor.

After designing the single metasurface near-eye visor, we design a pair of metasurfaces, where the second metasurface (located further from the eye) corrects any distortion of the real-world scene caused by the first metasurface. The gap size

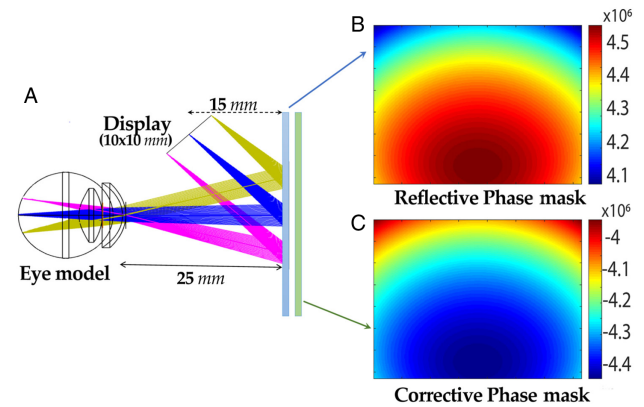


**Fig. 1.** Metaform visor. (A) Schematics of the metasurface NEV and its ray-tracing simulation in ZEMAX. (B) Reflective phase mask from the first metasurface of our visor. (C) Corrective phase mask for the second metasurface of our visor. The size of the visor is assumed to be  $4\text{ cm} \times 4\text{ cm}$ .

between two metasurfaces is assumed to be  $500\ \mu\text{m}$ , which is fixed to facilitate future fabrication on both sides of a glass wafer. The corrective phase mask of the second metasurface is also designed using Zernike standard polynomials. This phase mask is designed to minimize the RMS wavefront error [19] for light transmitted through two metasurfaces to ensure good see-through quality. Without using the corrective phase mask, the RMS wavefront error for light on the retina after passing through both metasurfaces is  $14.8\lambda$ . Such wavefront errors represent the see-through-quality, and with greater than wavelength rms error leads to a highly distorted view. However, after using the second metasurface to correct the distortion from the first metasurface, the RMS wavefront error is reduced to  $0.9\lambda$ . We also calculated the RMS wavefront error of a freeform visor developed in [20] to compare to our see-through quality. The RMS wavefront error of the freeform visor is  $1.17\lambda$ , which is better than that of a single metasurface but worse than that of our corrected composite metasurface visor.

Figure 1 shows the optimized metasurface NEV phase profiles, where the first metasurface (Fig. 1(B)) distorts the light field, but in conjunction with the second metasurface (Fig. 1(C)), the optical wavefront error is minimized. Once the phase functions are optimized, we implement them using metasurfaces, which is explained in more detail later in the paper.

We also evaluate the modulation transfer function (MTF) and the grid distortion cause by the NEV to estimate the image quality. The MTF of the system along the tangential and sagittal plane is shown in Fig. 2(A), exhibiting a value greater than 0.3 at 33 cycles/mm, which is a sufficient resolution for a human visual system [4] and satisfying the Nyquist resolution for a  $15\ \mu\text{m}$  pixel size. The grid distortion is less than 5.9%, which is sufficient for human intelligibility [4] (Fig. 2(B)). Additionally, we simulate an image of the green crossbars (based on our operating wavelength design) in Zemax to evaluate the see-through quality before and after using the second phase mask as shown in Fig. 2(C). The projected image of the crossbars is shown on the right side of Fig. 2(C), which is the image reproduced on the retina after passing through the phase masks and the eye model.

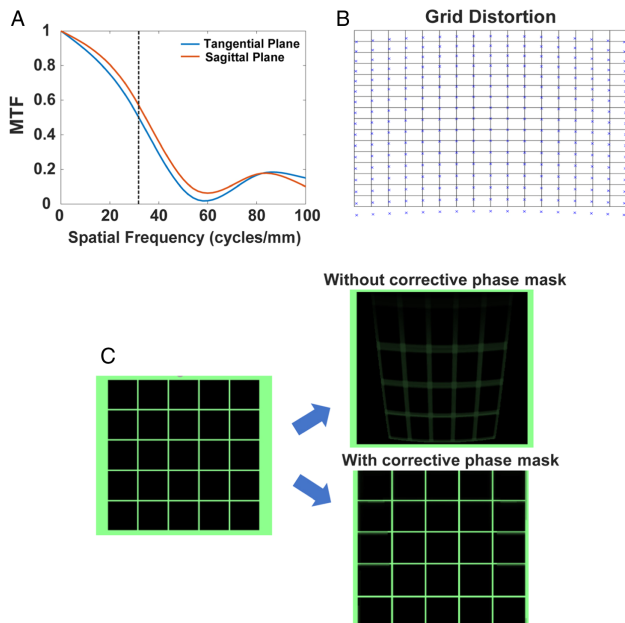


**Fig. 2.** (A) MTF of the NEV calculated in ZEMAX on the tangential and sagittal planes. (B) The grid distortion of the NEV corresponds to 10 mm  $\times$  10 mm display size. The highest calculated distortion is 5.9% at the corners. The corresponding operation wavelength here is 540 nm. (C) Image simulation of the green crossbars passing through the NEV using Zemax. The left figure is the original image that is seen in the real world. The right figure is the simulated image as seen by the person using the NEV before and after adding a corrective phase mask.

The image distortion is clearly observed without our corrective phase mask.

### 3. METASURFACE IMPLEMENTATION

So far, we assumed the NEV to be made of bilayer, ideal phase masks. In practice, these masks will be implemented using metasurfaces. The proposed stack of metasurfaces is shown in Fig. 3(A). The partially reflective metasurface is designed by placing silicon nitride nano-scatterers on a partially reflective distributed Bragg reflector (DBR) with two layers of silicon nitride and two layers of silicon oxide [21]. The resulting phase and amplitude of the reflected light as a function of pillar diameter (duty cycle) are shown in Fig. 3(B). Note that the amplitude of the reflected light is  $\sim 30\%$ , whereas the phase covers the full  $0 - 2\pi$  range. Engineering highly reflective silicon nitride metasurfaces without DBR is not trivial (due to the low refractive index of SiN) over the whole  $0 - 2\pi$  phase range, and using DBR layers helps us to increase this reflection efficiency up to 30% for the first metasurface while maintaining the full  $0 - 2\pi$  phase range. The second metasurface will be a transmissive one, whose transmission parameters are shown in Fig. 3(C). The sharp resonances observed in the phase and amplitude correspond to guided mode resonances and are excluded when designing the final metasurface by selecting pillar diameters off resonance. The design process involves selecting the appropriate spatial phase profile for the specific optical component, arranging the scatterers on a subwavelength lattice, and spatially varying their dimensions. The insets of Figs. 3(B) and 3(C) show cylindrical post formation, including their substrates. The DBR

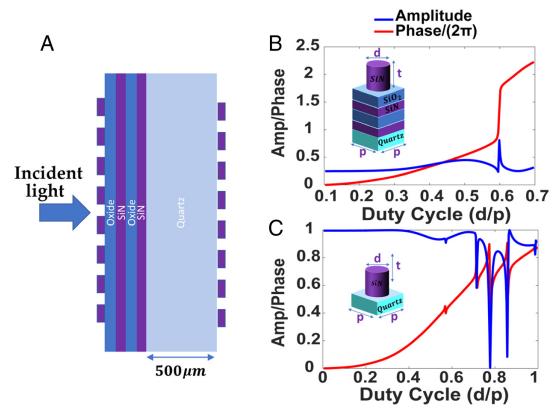


**Fig. 3.** Metasurface (MS) implementation of the phase masks: (A) schematic of the metasurface stack; the simulated phase and amplitude response of the (B) light reflected from the first metasurface and (C) light transmitted through the second metasurface. These plots are calculated using RCWA.

structure in Fig. 3(B) is designed for 540 nm wavelength, so its thickness is 67.5 nm for SiN and 90 nm for oxide. The metasurface periodicity  $p$  and thickness  $t$  for both metasurfaces here are set to 443 nm and 700 nm, respectively. The periodicity and thickness are chosen to maximize the transmission efficiency for second metasurface while maintaining the full  $0 - 2\pi$  phase coverage. All the simulations that we have done so far were for normal incident angle as shown in Fig. 3. However, based on our design schematic and display position in Fig. 1, our reflective metasurface will experience an angle of incidence from  $40^\circ$  to  $50^\circ$ . It is necessary for us to get the whole  $0 - 2\pi$  phase coverage at these angles as well, which is presented in more detail in Appendix A.

### 4. MULTIWAVELENGTH METASURFACE

One of the major issues facing metasurfaces is their strong chromatic aberrations. For example, a metalens will produce a focused image at one wavelength and an unfocused image at another [22]. A successful AR visor, however, must produce focused images at multiple wavelengths, specifically red, green, and blue, in order to display images for all perceivable colors. Much work has been done to produce multiwavelength achromatic metalenses (MAM) including multiplexing different functionalities in a single metasurface [23] or dispersion engineering [24], but until recently previous methods either have not been shown to work in the visible spectrum or have limitations on device size and the phase shift that can be imparted. Furthermore, such approaches have worked well for high-contrast scatterers (like silicon scatterers working in the infrared with refractive index  $n \sim 3.5$ ), as the light remains tightly confined inside the scatterer, and thus the coupling between different scatterers is minimized. Unfortunately, our application at visible wavelengths precludes silicon as the material of choice, and we have to rely on silicon nitride ( $n \sim 2$ ) and silicon dioxide ( $n \sim 1.5$ ), both of which are transparent and low-index materials relative to silicon. The method described in Ref. [25], however, showed that it is possible to produce a metalens that operates at discrete wavelengths with large differences in the required phase shift at each wavelength. Our metasurface design

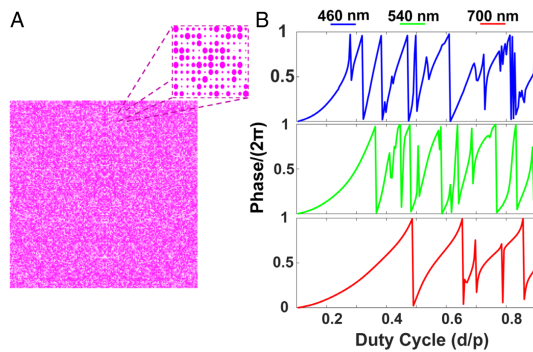


**Fig. 4.** (A) Final radii distribution of our multiwavelength reflective metasurface visor using our optimization method. The diameter of the nanopillars changes from 46 to 398 nm. (B) Phase of the reflected light through a scatterer using RCWA as a function of the duty cycles of the nanopillar at wavelengths of 460, 540, and 700 nm. As the pillar width changes, the corresponding phase undergoes multiple  $0 - 2\pi$  phase cycles. The sharp phase jumps reflect the excitation of guided mode resonance (GMR).

employs this same method and demonstrates that guided mode resonances (GMR) can give rise to numerous  $0 - 2\pi$  phase-shift cycles observed for the duty cycle range for pillars using silicon nitride.

Our metasurface visor has a target phase profile at each wavelength that is position dependent. The pillar at any position on the visor must match the desired phases of all three wavelengths [R (700 nm), G (540 nm), B (460 nm)] at that position simultaneously. Typically, for a monochromatic metasurface, when the phase shift of a pillar is chosen, the phase that it imparts at other wavelengths is then determined as well. Said another way, for a given phase shift, there is typically only one corresponding pillar size at each wavelength that imparts that phase shift. However, by scatterer design, we can have multiple pillar sizes at each wavelength that impart the desired phase shift. This enables us to better match phase profiles at different wavelengths, as we can keep the phase shift at one wavelength fixed while selecting a different pillar size that may better match the phase profile at another wavelength. This one-to-many relationship between phase and pillar size is achieved by choosing pillar parameters such that the imparted phase shift spans  $0 - 2\pi$  multiple times over the range of possible pillar sizes (Fig. 4). The greater the number of  $0 - 2\pi$  cycles at each wavelength, the better we can design a metasurface that matches the phase profiles of all wavelengths. This approach is aided by the occurrence of GMR, which causes sudden, abrupt phase shifts that increase the number of pillar sizes available to fulfill a target phase shift.

Using rigorous coupled wave analysis (RCWA) [26], reflection coefficients and phases for pillars ranging in diameter from 10% to 90% of the periodicity were calculated for each wavelength. The lattice periodicity  $p$  and thickness  $t$  at all wavelengths here are set to 443 nm and 1500 nm, respectively, to achieve multiple  $0 - 2\pi$  cycles at all three wavelengths. Pillars with reflection coefficients below 0.3 at any wavelength were removed from consideration, as we want to strike a balance between transmission and reflection to maintain a partially reflective visor. For each discretized position in a phase mask, the remaining pillars were assigned an error weight calculated as the square of the difference between the phase mask at that position

**Table 1.** AR Visor Performance in Terms of MTF Before and After RGB Optimization

Wavelength (nm)	460	540	700
Single wavelength metasurface visor (cycles/mm)	0.61	0.49	0.53
Multiwavelength metasurface visor (cycles/mm)	0.51	0.47	0.49

and the pillar's phase shift at that phase mask's wavelength. The metasurface in our proposed structure was then designed by selecting pillars with the smallest cumulative error ( $\epsilon$ ) across the three phase masks at each position, which is given by

$$\epsilon(x, y, r) = \sum_{i=1}^n \sqrt{(\phi(x, y, \lambda_i) - f(r, \lambda_i))^2},$$

where  $(x, y)$  is the position on the phase mask,  $\lambda_i$  is the design wavelength,  $r$  is the pillar radius, and  $n$  is the number of wavelengths (here  $n = 3$ ). The desired phase is given by  $\phi$ , and the calculated phase shift for each pillar is given by  $f$ . The final radii distribution of our multiwavelength reflective metasurface visor is shown in Fig. 4(A). We emphasize that, in this method, we are primarily designing a metasurface that works at certain specific wavelengths, and true broadband operation is not expected. Hence, we need to rely on a display that supports only discrete wavelengths, such as a laser-based display [27].

We then validated our design of a reflective metasurface visor by importing the phase profiles that are provided by our final optimized scatterer distribution into the NEV structure via ray optic simulation, which is shown in Fig. 1. Table 1 provides the MTF for three colors at 33 cycles/mm (via Zemax). The MTFs for the multiwavelength metasurface are comparable to that of the monochrome design, exhibiting minimal degradation in performance. This clearly demonstrates that the multicolor metasurface does not degrade the performance of the visor compared to monochrome metasurface one.

We also analyzed the bandwidth of the light source for the display, and we found that the MTF does not fall very quickly and at least works for over a  $\sim 20$  nm bandwidth. We define the bandwidth by the range of wavelengths over which the MTF exceeds 0.3 at 33 cycles/mm (Appendix B). Hence, in some cases, we also can use a narrowband light-emitting diodes (LEDs), such as an organic LED, instead of a laser for the display.

Once we finalize the multiwavelength reflective visor design, we then optimize the design for the second metasurface at the central wavelength. We found that while the second metasurface is designed to negate the effect of the first metasurface, such negation happens over the full simulated wavelength range. As can be seen in Fig. 5, the RMS wavefront error is minimal over a broad optical bandwidth (simulated for different angles).

Additionally, we simulate an image of the white crossbars in Zemax to evaluate the see-through quality as shown in Fig. 5(B). The projected image of the crossbars is shown on the right side of Fig. 5(B), which is the image reproduced on the retina after passing through the metasurface layers and the eye model. We can

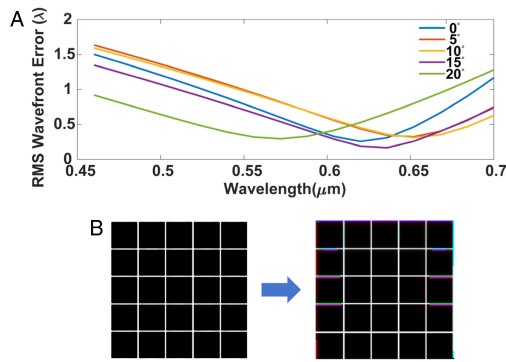


**Fig. 5.** (A) RMS wavefront error in the visible range calculated for the transmitted light through the visor (light that passes through two metasurfaces) in five different incident angles. (B) Image simulation of the white crossbars passing through NEV using Zemax. The left figure is the original image that is seen in the real world. The right figure is the simulated image as seen by the person using the NEV.

clearly observe that the rainbow effect caused by chromatic aberration of these metasurfaces is negligible.

## 5. DISCUSSION

The proposed composite metasurface visor can overcome the bulkiness, FOV limitations, chromatic aberrations, and see-through quality of existing NEVs. Using our proposed structure, we can make the eyewear devices flat, ultrathin, and close to eye, while maintaining a large FOV for the virtual world. However, there are some challenges with the current design, including a small eye box, scattered light from possible back reflection, and large-area fabrication. The eye box for our current visor is  $2.5 \text{ mm} \times 2.5 \text{ mm}$  (denoting exit pupil diameter without any expansion), which is lower than that of current waveguide-based visors [28], although there are some solutions to increase the eye box by multiplexing different phase masks into one metasurface [29]. In addition, there could be some additional noise due to the back-reflected light from a second metasurface. However, our second metasurface is designed to be fully transmissive ( $>98\%$ ) as shown in Fig. 3(C). To mitigate the impact of this possible  $<2\%$  back reflection from the second metasurface in future work, we can apply an antireflection coating incorporated with our scatterers or instead employ a modified scatterer design to maximize this to  $>99\%$  transmission. A complete stray light analysis is warranted to establish the efficacy of our method for building NEV. A full-wave stray light analysis of the actual NEV, however, is not feasible owing to its large size. Hence, we instead used a combination of RCWA and ray optics simulation in this paper, which together show little effects from the stray light.

Another remaining issue is fabrication. While the fabrication of the current design is challenging, fabrication methods already exist that show that such large-area fabrication using deep ultraviolet (DUV) lithography [30] is possible with high throughput. We also have simulated the tolerance of the metasurfaces to lateral misalignment in terms of acceptable RMS wavefront error range (Appendix C).

We can also increase the efficiency of our current design by making our visor reflective only at certain display angles

and totally transmissive at all other angles. Another limitation of the current proposed metasurface visor will be the vergence-accommodation conflict (VAC), which is common in current AR glasses. However, a recent study shows that, by using a tunable focal length lens, the VAC can be reduced [31,32]. By integrating metasurface structures into micro-electromechanical systems, such tunability can be achieved, which can mitigate the VAC [33,34].

## 6. CONCLUSION

Our work explored the possibility of using a metasurface to design and create a compact near-eye visor that provides a large FOV and also reasonable see-through quality for an immersive AR experience. The proposed metasurface visor does not suffer from chromatic aberrations, while providing a large display field of view ( $>77^\circ$  both horizontally and vertically), and good ( $>70\%$  transmission and no distortion) see-through quality.

The current visor includes two layers of metasurfaces, which have different phase masks. The scatterers in the metasurface near the eye (which is reflecting the virtual world to the eye) are designed to have 30% reflectivity and multi-chrome behavior, whereas the scatterers in the metasurface further from the eye (which help improve the see-through quality) are designed to have close to 100% transmission. The main idea behind our multi-chrome behavior is that we start with the desired phase profiles for each color and then find the scatterer distribution that provides the phase profiles closest to the desired one.

In this work, we focused on design and simulation of the whole AR metasurface visor due to the complexity of design. Additionally, there are many other relevant factors for high-quality immersive AR experience including large eye box, high efficiency, broadband operation, and tunability (to mitigate VAC) which are not specified in our current architecture. However, we believe that the demonstrated multilayer metasurface visor is capable of addressing those issues.

## APPENDIX A: ANGLE DEPENDENCY

All the RCWA simulations for the phase and amplitude calculation (in reflection and transmission mode) were performed under normal incidence as shown in Fig. 3. However, based on our design schematic and display position in Fig. 1, our reflective metasurface will experience an angle of incidence from  $40^\circ$  to  $50^\circ$ . It is necessary for us to get the whole  $0 - 2\pi$  phase coverage at these angles as well. As it is shown in Fig. 6, at these angles we still get multiple wraps of  $0 - 2\pi$  phase change, which is ideal for our multiwavelength design approach. Here the operation wavelength for angle dependency simulation is 540 nm, and all of the incoming light is assumed to be transverse-electric (TE) polarized beams.

## APPENDIX B: BANDWIDTH TOLERANCE

As we mentioned in Section 4, we have primarily designed a metasurface that works at certain specific wavelengths, and true broadband operation is not expected here. However, we also analyzed the bandwidth of the light source for the display, and we found that the MTF does not fall very quickly and at least

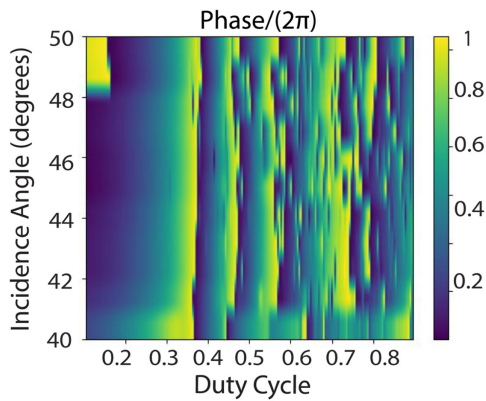


**Fig. 6.** Angle dependency RCWA simulation from 0 to  $2\pi$  for one wavelength (540 nm). The duty cycle is defined as the ratio of the post diameter to the periodicity. The parameters of the pillars are the same as in Fig. 3.

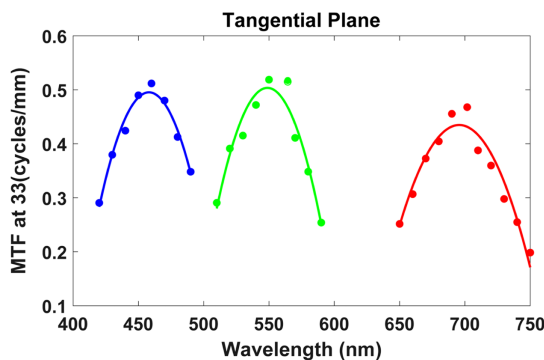


**Fig. 7.** MTFs of the blue, green, and red colors for the reflective visor at 33 cycles/mm in the tangential plane. MTFs above 0.3 at 33 cycles/mm are our evaluation point for acceptable bandwidth.

works for over a  $\sim 20$  nm bandwidth. We define the bandwidth by the range of wavelengths over which the MTF exceeds 0.3 at 33 cycles/mm (Fig. 7). Hence, we can use an LED instead of a laser for the display.

### APPENDIX C: FABRICATION TOLERANCE

While the fabrication of the proposed design is challenging, we note that the DUV lithography-based fabrication [30] method can reach the smallest features used in our paper. Thus, there is a clear pathway for high-throughput large-area fabrication. Two metasurfaces will be fabricated on opposite sides of a 500  $\mu\text{m}$  thick quartz substrate. Silicon-nitride film will be deposited on both sides of the substrate using plasma-enhanced chemical vapor deposition (PECVD). One of the challenging tasks will be to align two metasurfaces during fabrication on both sides of a quartz substrate. To solve this, we will also create registration alignment marks on both side of the substrate using photolithography and an ABM aligner. The reflective metasurface (Metasurface I) pattern will be exposed via electron-beam lithography on one side of the sample. After the lithography step, a layer of aluminum will be evaporated onto the sample. After performing liftoff, the sample will be etched using an

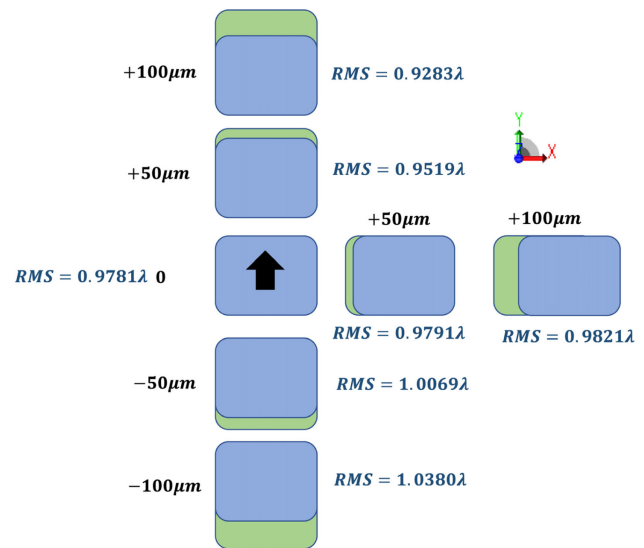


**Fig. 8.** Analysis of lateral tolerance in terms of the RMS wavefront error in the transmitted light. Up to  $\sim 100$   $\mu\text{m}$  misalignment, the error remains below one wavelength. The operation wavelength here is 540 nm, and the angle of incidence is assumed to be normal. The blue box represents the first metasurface (reflective phase mask), and the green represents the second metasurface (corrective phase mask). The arrow mark shows us which side of the metasurface is up compared to our eye view.

inductively coupled plasma etcher, and the remaining aluminum will be removed in a photoresist developer. To protect the patterns from mechanical damage during the processing of the other side of the sample, a thick layer of SU-8 polymer will be spin-coated over the nanoposts, yielding a rigid planarized layer that will encapsulate and protect the nanoposts. The corrective metasurface (Metasurface II) will be fabricated on the other side of the substrate using the same processing steps as used for the fabrication of Metasurface I. In Fig. 8, we have simulated the tolerance of the metasurfaces to lateral misalignment. In this test simulation, the operation wavelength is 540 nm, and the angle of incidence is assumed to be normal. We are looking for changes in RMS wavefront error in see-through mode. We found out that, up to 100  $\mu\text{m}$  misalignment, the error remains below one wavelength, which is still close to our current RMS at normal incident angle.

**Funding.** Samsung Global Research Outreach (GRO); UW Reality Lab; Facebook; Google; Futurewei.

**Acknowledgment.** We thank the Optics Studio (Zemax) corporation for the available ray-tracing simulation and optimization method.

**Disclosures.** The authors declare no conflicts of interest.

### REFERENCES

1. R. Azuma, Y. Baillet, R. Behringer, S. Feiner, S. Julier, and B. MacIntyre, "Recent advances in augmented reality," *IEEE Comput. Graph. Appl.* **21**, 34–47 (2001).
2. X. Hu and H. Hua, "High-resolution optical see-through multi-focal-plane head-mounted display using freeform optics," *Opt. Express* **22**, 13896–13903 (2014).
3. J. W. Pan, C. Che-Wen, K. D. Huang, and C. Y. Wu, "Demonstration of a broad band spectral head-mounted display with freeform mirrors," *Opt. Express* **22**, 12785–12798 (2014).

4. J. Yang, P. Twardowski, P. Gérard, and J. Fontaine, "Design of a large field-of-view see-through near to eye display with two geometrical waveguides," *Opt. Lett.* **41**, 5426–5429 (2016).
5. Z. Liu, C. Pan, Y. Pang, and Z. Huang, "A full-color near-eye augmented reality display using a tilted waveguide and diffraction gratings," *Opt. Commun.* **431**, 45–50 (2019).
6. T. Yoshida, K. Tokuyama, Y. Takai, D. Tsukuda, T. Kaneko, N. Suzuki, T. Anzai, A. Yoshikaie, K. Akutsu, and A. Machida, "A plastic holographic waveguide combiner for light-weight and highly-transparent augmented reality glasses," *J. Soc. Inf. Disp.* **26**, 280–286 (2018).
7. B. C. Kress, "Optical waveguide combiners for AR headsets: features and limitations," *Proc. SPIE* **11062**, 110620J (2019).
8. J. D. A. Waldern, J. Grant, and M. M. Popovich, "DigiLens switchable Bragg grating waveguide optics for augmented reality applications," *Proc. SPIE* **10676**, 106760G (2018).
9. N. Yu and F. Capasso, "Flat optics with designer metasurfaces," *Nat. Mater.* **13**, 139–150 (2014).
10. A. Zhan, S. Colburn, C. M. Dodson, and A. Majumdar, "Metasurface freeform nanophotonics," *Sci. Rep.* **7**, 1673 (2017).
11. W. Stork, N. Streibl, H. Haidner, and P. Kipfer, "Artificial distributed-index media fabricated by zero-order gratings," *Opt. Lett.* **16**, 1921–1923 (1991).
12. C. Hong, S. Colburn, and A. Majumdar, "Flat metaform near-eye visor," *Appl. Opt.* **56**, 8822–8827 (2017).
13. G. Y. Lee, J. Y. Hong, S. Hwang, S. Moon, H. Kang, S. Jeon, H. Kim, J.-H. Jeong, and B. Lee, "Metasurface eyepiece for augmented reality," *Nat. Commun.* **9**, 4562 (2018).
14. S. Lan, X. Zhang, M. Taghinejad, S. Rodrigues, K. T. Lee, Z. Liu, and W. Cai, "Metasurfaces for near-eye augmented reality," *ACS Photon.* **6**, 864–870 (2019).
15. S. Moon, C. K. Lee, S. W. Nam, C. Jang, G. Y. Lee, W. Seo, G. Sung, H.-S. Lee, and B. Lee, "Augmented reality near-eye display using Pancharatnam-Berry phase lenses," *Sci. Rep.* **9**, 6616 (2019).
16. S. M. Kamali, E. Arbabi, and A. Faraon, "Metasurface-based compact light engine for AR headsets," *Proc. SPIE* **11040**, 1104002 (2019).
17. D. A. Atchison and G. Smith, *Optics of the Human Eye* (Butterworth-Heinemann, 2000).
18. V. F. Zernike, "Beugungstheorie des schneidenverfahrens und seiner verbesserten form, der phasenkontrastmethode," *Physica* **1**, 689–704 (1934).
19. R. R. Shannon, *Optical Specification. Handbook of Optics* (1995), Vol. 1, p. 35-1.
20. D. Cheng, H. Hua, and Y. Wang, "Optical see-through free-form head-mounted display," U.S. patent 13/318,864 (17 September 2012).
21. C. J. R. Sheppard, "Approximate calculation of the reflection coefficient from a stratified medium," *J. Eur. Opt. Soc. A* **4**, 665 (1995).
22. S. Colburn, A. Zhan, and A. Majumdar, "Metasurface optics for full-color computational imaging," *Sci. Adv.* **4**, eaar2114 (2018).
23. E. Arbabi, A. Arbabi, S. M. Kamali, Y. Horie, and A. Faraon, "Multiwavelength metasurfaces through spatial multiplexing," *Sci. Rep.* **6**, 32803 (2016).
24. W. T. Chen, A. Y. Zhu, and F. Capasso, "Flat optics with dispersion-engineered metasurfaces," *Nat. Rev. Mater.* **5**, 604–620 (2020).
25. Z. Shi, M. Khorasaninejad, Y. W. Huang, C. Roques-Carnes, A. Y. Zhu, W. T. Chen, V. Sanjeev, Z. W. Ding, M. Tamagnone, K. Chaudhary, and R. C. Devlin, "Single-layer metasurface with controllable multiwavelength functions," *Nano Lett.* **18**, 2420–2427 (2018).
26. V. Liu and S. Fan, "S4: A free electromagnetic solver for layered periodic structures," *Comput. Phys. Commun.* **183**, 2233–2244 (2012).
27. K. V. Chellappan, E. Erden, and H. Urey, "Laser-based displays: a review," *Appl. Opt.* **49**, F79–F98 (2010).
28. J. M. Miller, N. De Beaucoudrey, P. Chavel, J. Turunen, and E. Cambriil, "Design and fabrication of binary slanted surface-relief gratings for a planar optical interconnection," *Appl. Opt.* **36**, 5717–5727 (1997).
29. S. B. Kim and J. H. Park, "Optical see-through Maxwellian near-to-eye display with an enlarged eyepiece," *Opt. Lett.* **43**, 767–770 (2018).
30. J. S. Park, S. Zhang, A. She, W. T. Chen, P. Lin, K. M. Yousef, J. X. Cheng, and F. Capasso, "All-glass, large metalens at visible wavelength using deep-ultraviolet projection lithography," *Nano Lett.* **19**, 8673–8682 (2019).
31. N. Padmanaban, R. Konrad, T. Stramer, E. A. Cooper, and G. Wetzstein, "Optimizing virtual reality for all users through gaze-contingent and adaptive focus displays," *Proc. Natl. Acad. Sci. USA* **114**, 2183–2188 (2017).
32. Y. J. Wang, Y. H. Lin, O. Cakmakci, and V. Reshetnyak, "Varifocal augmented reality adopting electrically tunable uniaxial plane-parallel plates," *Opt. Express* **28**, 23023–23036 (2020).
33. Z. Han, S. Colburn, A. Majumdar, and K. Bohringer, "MEMS-actuated metasurface Alvarez lens," arXiv:2001.07800 (2020).
34. E. Arbabi, A. Arbabi, S. M. Kamali, Y. Horie, M. Faraji-Dana, and A. Faraon, "MEMS-tunable dielectric metasurface lens," *Nat. Commun.* **9**, 812 (2018).